LMIRcam: an L/M-band imager for the LBT combined focus

John C. Wilson[a], Philip M. Hinz[b], M. F. Skrutskie[a], Terry Jones[c], Elliott Solheid[b], Jarron Leisenring[a], Peter Garnavich[d], Matthew Kenworthy[b], Matthew J. Nelson[a] and Charles E. Woodward[c]

[a]University of Virginia, 530 McCormick Rd, Charlottesville, VA, 22904, USA;
[b]University of Arizona, 933 N. Cherry Ave, Tucson, AZ, 85721, USA;
[c]University of Minnesota, 116 Church St SE, Minneapolis, MN, 55455, USA;
[d]University of Notre Dame, 225 Nieuwland Science, Notre Dame, IN, 46556, USA

ABSTRACT

The L/M-band mid-InfraRed Camera (LMIRcam) will use a mid-wave (5.1 μm cut-off) Teledyne Imaging Systems HgCdTe HAWAII 1-RG array to image the coherently combined (Fizeau) focus of the Large Binocular Telescope's twin 8.4-meter primary mirrors generated by the University of Arizona's beam combiner — the Large Binocular Telescope Interferometer (LBTI). The 1024x1024 array will have a pixel scale of 10.9 milliarcsec (mas) per pixel and a field of view of 10"x10". The highest achievable angular resolution will be 26 mas (34 mas) for 3.6 μm (4.8 μm). LMIRcam will operate in parallel with the Nulling Infrared Camera (NIC), sharing the same Dewar. In addition to a suite of broad and narrow-band filters, LMIRcam will contain grisms for low-resolution spectroscopy, and serve as a test-bed for novel pupil masks to enable high-contrast imaging. The opto-mechanical design, anticipated performance, and a sample of potential science applications are presented. LMIRcam is funded by the National Science Foundation and the University of Virginia.

Keywords: Infrared, Interferometry, Fizeau, Biconics, SPDT

1. INTRODUCTION

The Universities of Arizona, Minnesota, Notre Dame, and Virginia are collaborating in the development of an L (3.6 μm) and M (4.8 μm) Fizeau imager, the L/M-band mid-InfraRed Camera (LMIRcam), to operate behind the Arizona led Large Binocular Telescope Interferometer[1] (LBTI) beam combiner at the Large Binocular Telescope (LBT) at Mt. Graham, Arizona. With a 10.9 mas pixel pitch, the camera will take full advantage of the 22.8 meter baseline of the two 8.4 meter mirrors of the LBT to deliver a first interferometric null 26 mas (34 mas) from the PSF core working at a wavelength of 3.6 μm (4.8 μm). In addition to imaging capability in the atmospheric L and M broadbands, the instrument will have narrowband filters tuned to water ice, hydrogen line emission/absorption, and polycyclic aromatic hydrocarbon (PAH) features, and it will provide R $\sim$ 400 grism spectroscopy in the L and M bands. LMIRcam's detector will be a 1024x1024 mid-wave (5.1μm cut-off) Teledyne Imaging Systems HgCdTe HAWAII-1RG array. LBTI serves as the beam combiner for both the Nulling Infrared Camera[2] (NIC), the original nulling imager for the NASA funded LBTI project which operates primarily in the 8 – 13 μm atmospheric window, and LMIRcam, which shares the same Dewar with NIC, allowing the potential for simultaneous operations since they share a dichroic within the Dewar that sends the appropriate wavelength light to each instrument.

Our current activities include tolerancing the optical design, determining filter specifications, opto-mechanical design of optics mounts and filter/stop wheels, and initial fabrication. The LMIRcam opto-mechanics and detector will be integrated with the NIC Dewar at the University of Arizona in Summer 2009. The combined instruments will be tested on the MMT on Mt. Hopkins late in 2009. First light at LBT will follow in 2010-2011.

Further author information: (Send correspondence to J.C.W.)
J.C.W.: E-mail: jcw6z@virginia.edu, Telephone: 1 434 924 4907

Optical and Infrared Interferometry, edited by Markus Schöller, William C. Danchi, Françoise Delplancke
Proc. of SPIE Vol. 7013, 70133A, (2008) · 0277-786X/08/$18 · doi: 10.1117/12.789939

Downloaded from SPIE Digital Library on 13 Jul 2011 to 150.135.115.80. Terms of Use: http://spiedl.org/terms

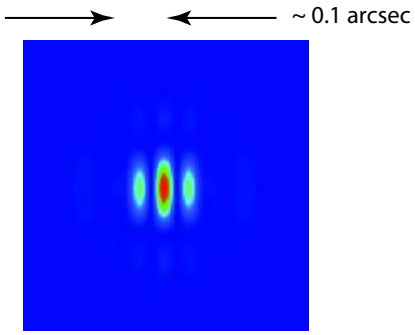

Figure 1. The predicted LBTI PSF. The first null is located at $\frac{\lambda}{2D}$ corresponding to 26 mas at 3.6 μm and 34 mas at 4.8 μm.

2. OPTICAL DESIGN

The combination of the dual adaptive secondary mirrors for LBT with the LBTI beam combiner will yield near diffraction-limited images at the combined Fizeau focus (Figure 1) which occurs just inside the NIC Dewar. Since the LBT pupil is a convolution of a single 8.4 meter aperture with a pair of delta-functions with 14.4 meter separation, the vertical axis of the image represents an Airy disc of a single 8.4 meter aperture while the horizontal axis is the product of that Airy disc with a two slit diffraction pattern. For this configuration the secondary peak intensity is 42 % of the primary peak. The first null is located at $\frac{\lambda}{2D}$ corresponding to 26 mas at 3.6 μm and 34 mas at 4.8 μm. Strehl ratio is anticipated to exceed 80 % at 3.6 μm and 90 % at 4.8 μm routinely, with performance improving with seeing conditions.

The requirements of the imaging train were to provide an intermediate focus for the placement of a field stop, slits for spectroscopy, and coronagraphic masks if desired, a reimaged pupil for stray light rejection and placement of filters, and finally a focus at the H1RG detector. A second reimaged pupil is naturally produced upstream of the detector where the grisms will be placed. The LBTI beam combiner delivers a common envelope beam of f/15 derived from individual f/41.2 beams from the two telescopes. LMIRcam uses 1:1 reimaging to provide a plate scale of 10.9 mas/pixel, which is a good match to the L- and M-band PSF.

The FOV at the LBTI combined focus is 40"x60". LMIRcam will operate with a 1024x1024 detector at first-light giving a 10"x10" FOV within the 40"x60" LBTI FOV. The optical design, however, will accommodate the optical paths required to operate an unvignetted 2048x2048 detector, with the expectation that a larger format array may become available in the future.

A custom dichroic positioned immediately after the LBTI combined focus will transmit 3 – 5 μm light to LMIRcam and reflect both 7 – 25 μm light into the NIC optical train and near-infrared light for phase sensing to correct path length within LBTI.

The optical design places all of the optical power in two diamond-turned biconic mirrors simplifying the overall layout and enabling a folded design that easily fits in the compact space available for the instrument. The optics produce an intermediate focal plane and two pupil positions. The availability of two pupils enables both the placement of filters and grisms as well as phase masks for more sophisticated suppression of diffracted light. Figure 2 shows a simplified (unfolded) optical layout for the system. The optics were designed using the ZEMAX^{TM}optical design program.*

Biconic mirrors have a different radius of curvature and conic constant in each of the x and y dimensions. They are so-called 'free-form' optics which do not exhibit rotational symmetry.[3] The biconics simplify the LMIRcam optical train by combining the action of a powered element and fold mirror while correcting for astigmatism and defocus through the different x and y prescription. Each biconic in LMIRcam tips the beam by ~ 7 deg. This tilt of the beam in one axis requires the radius of curvature in that axis to be slightly longer (~ 1.5 % for each

*ZEMAX Development Corporation, Bellevue, WA; www.ZEMAX.com

Downloaded from SPIE Digital Library on 13 Jul 2011 to 150.135.115.80. Terms of Use: http://spiedl.org/terms

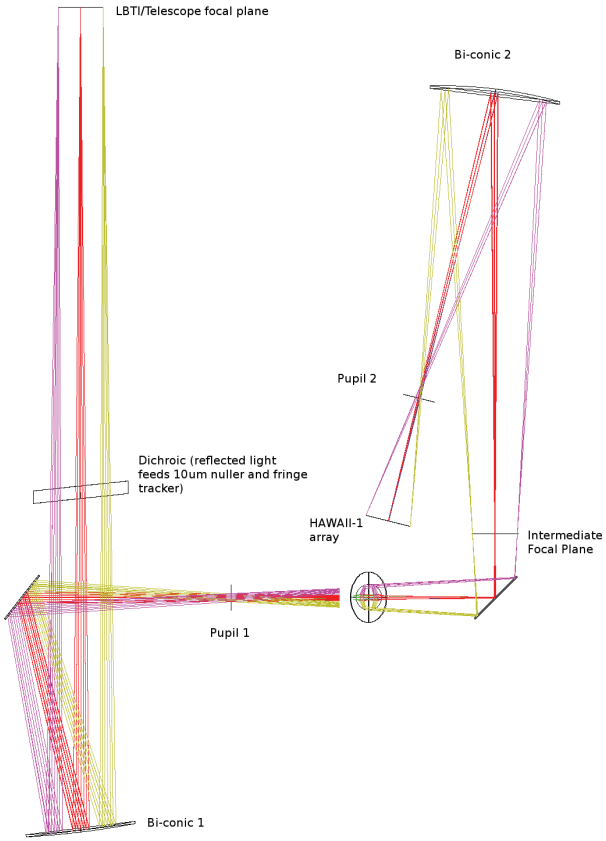

Figure 2. LMIRcam optical design. The layout has had a fold mirror removed and one-half of the optical train has been re-oriented by 90 deg in order to put all of the ray paths in the same plane for illustrative purposes.

biconic) than the radius of curvature in the other axis. Optimization shows that performance improves when each axis has a slightly different conic constant as well. This design was selected after first trying to use only conic sections for the powered elements which resulted in more elements that would take up additional space and make optical alignment more difficult.

Because biconics do not exhibit rotational symmetry they must be fabricated using single point diamond turning (SPDT) machines with a fast-tool servo or by raster fly-cutting. A fast-tool servo translates the cutting tool along the direction parallel to the diamond-turning machine axis as a function of radius from the center of the part and rotation angle. LMIRcam will be able to take advantage of the excellent research and development on diamond-turned biconics accomplished for the Infrared Multi-Object Spectrometer (IRMOS) instrument.[4] The specifications for the LMIRcam optics are listed in Table 1. Both biconics are on-axis (no decenter of the optical axis with respect to the part) and have circular apertures. Both biconics will be made from 6061-T6 aluminum alloy, the same alloy used for the opto-mechanical assemblies and optical bench, with a 6:1 (diameter:thickness) aspect ratio.

2.1 Tolerancing

Strehl ratio of the PSF's delivered to LMIRcam by the telescope and LBTI beam combiner are expected to be 80 % (90 %) at 3.6 μm (4.8 μm). To maintain this excellent performance, LMIRcam was required not to degrade the delivered Strehl ratios by more than 5 %. The EE-version of ZEMAX^{TM}was used to tolerance the optical design sensitivity to manufacturing and alignment errors and set opto-mechanical specifications to meet this performance requirement.

Downloaded from SPIE Digital Library on 13 Jul 2011 to 150.135.115.80. Terms of Use: http://spiedl.org/terms

Table 1. Biconic Specifications.

	Clear Aperture Dia (mm)	Y-radius (mm)	Y-conic	X-radius (mm)	X-conic
Biconic 1	100	−645.034	−0.449	−654.757	−0.424
Biconic 2	134	−347.288	−0.164	−352.503	−0.152

A tolerance of ±0.127 mm (±5 mils) was assigned to parameters such as element thicknesses, airspaces, translational displacements of optics and optical decenters. A tolerance of 0.0167 deg (1 arcmin) was assigned to parameters such as optical and mechanical tilts. Lastly, surface figure [†] (ZEMAX tolerance operand TIRR) and irregularity (ZEMAX tolerance operand TEZI with coefficients 4 – 10) of optics with flat surfaces (e.g. dichroics and fold mirrors) were assigned 29 nm RMS. This is very conservative considering these flat surfaces will probably be fabricated with traditional polishing techniques.

Ultimately surface roughness should be specified such that signal is not significantly degraded. A surface roughness of 15 nm RMS distributed over 10 surfaces gives an acceptable 5 % loss of signal. Table 2 summarizes these 'global' tolerances. While the 3 – 5 μm thermal background will dominate other scattered light sources, it is useful to consider the relative scattering importance of surface roughness and particulates within LMIRcam. Both surface roughness of 3 nm RMS and contamination level 300 (254 ppm) give comparable scattering contributions at and around 2 μm.[‡] Scatter from 15 nm RMS surfaces, with total integrated scatter (TIS; Ref. 5) a factor of 25 more than 3 nm RMS surfaces, should exceed particulate scattering.

Table 2. Global tolerance values used in LMIRcam with the exception of biconics.

Tolerance Type	Value
Element thicknesses, airspaces, displacements, decenters	±0.127 mm (±5 mils)
Optical & mechanical tilts	0.0167 deg (1 arcmin)
Flat surface figure & irregularity	15 nm

There are currently no operands provided within ZEMAX that can be used to directly tolerance the surface figure[§] of biconic surfaces. To tolerance surface figure within ZEMAX the surface definition was changed from Biconic to Biconic Zernike using the first 10 Zernike coefficients. ZEMAX uses the Zernike set defined by Ref. 6 for the Biconic Zernike surface. Each coefficient was set to zero in the nominal design. For tolerancing, coefficients 4 – 10 were assigned an identical tolerance of ±50 nm. The maximum RMS is therefore ∼ 130 nm, the root-sum-square of the seven coefficients. This is ∼ $\lambda/5$ RMS at 0.6328 nm. Zernikes 1 – 3 where not used because it is assumed piston and tip-tilt errors can be accommodated with the placement of the detector. Truncation at coefficient 10 comes from an expectation that up to ∼ 10 Zernike coefficients can be fit during interferometric testing during fabrication[¶].

Not included in the ZEMAX analysis is the change in surface figure when the biconic mirrors are cooled to 77 K. Ref. 7 investigated the effect of various mechanical stress relieving procedures on diamond-turned flat and spherical mirrors fabricated from 6061-T651 aluminum plate stock. A control spherical mirror with no stress relief processing changed on average ∼ 0.13 λ RMS (at He-Ne) surface error from room temperature to cryogenic temperatures over three cooldowns. The stress relieved spherical mirror with the least change (their procedure SR5) had on average ∼ 0.065 λ RMS surface figure error change, mostly astigmatism. The spherical test mirror that underwent SR5 in Ref. 7 had average (over three cooling cycles) surface error changes due to 45 deg (0,90 deg) astigmatism of 42 (32.8) nm RMS measured over a maximum diameter sub-aperture. To take

[†] Defined to be spatial wavelengths $\lambda_D > 1$ mm.

[‡] Gary Peterson, personal communication.

[§] Defined to be spatial wavelengths $\lambda_D < 100\,\mu$m.

[¶] Alex Sohn, personal communication.

Downloaded from SPIE Digital Library on 13 Jul 2011 to 150.135.115.80. Terms of Use: http://spiedl.org/terms

this error into account it is conservatively assumed that this surface figure change will be manifested primarily as additive zernike terms for astigmatism. Assuming the LMIRcam mirrors suffer this change across the entire clear aperture, the fabricated surface error would need to be tightened to 94 nm RMS to result in the desired 130 nm RMS upon cooling. For added contingency the LMIRcam biconic surface figure requirement is tightened further to 63 nm RMS ($\lambda/10$ RMS at He-Ne).

Table 3. Biconic Tolerances.

	Biconic 1	**Biconic 2**
Y Radius	$\pm 0.1\,\%$	$\pm 1\,\%$
Y Conic Constant	± 0.05	± 0.05
Ratio of Radii (X Radius/Y Radius)	$\pm 0.05\,\%$	$\pm 0.1\,\%$
X Conic Constant	± 0.05	± 0.05
RMS Surface Figure	63 nm	63 nm
RMS Surface Roughness	15 nm (Best Effort)	15 nm (Best Effort)

A means of tolerancing surface roughness for the biconics could not readily be found within ZEMAX. Nonetheless, as discussed above, a surface roughness of 15 nm RMS for the biconics, as with the other surfaces, gives an acceptable 5 % loss of signal. The typical roughness attainable with diamond-turned optics will be sufficient for our needs. The biconic mirrors machined as part of the IRMOS project had surface roughness of 16 nm (fabricated with SPDT and fast-tool servo at the Precision Engineering Center at North Carolina State University, Raleigh, NC) and 11 nm (fabricated with raster fly-cutting at the Labor fuer Mikrozerspanung (LFM) at the University of Bremen, Germany).[4]

SPDT typically creates concentric tool marks that could produce scattered light by diffracting light out of the direction of specular reflection and into higher orders. This diffraction is not expected to be a problem within LMIRcam. A simple check using PCGRATE-1E$^{\mathrm{TM}}$software[‖] showed that diffraction efficiency in first order assuming 7 deg angle of incidence, 30 μm groove period and 90 nm groove depth (see Figure 4a in Ref. 8) in a triangular groove shape was $< 0.4\,\%$ at 3 μm, about the same as the TIS expected from 15 nm surface roughness at 3 μm. In addition, the pupils which follow each biconic will effectively baffle the diffracted light from reaching the detector.

The ratio of the radii of curvature for the two biconics was also toleranced. More accurately, the multiplicative scale factor f where the radius of curvature for biconic 2 is f multiplied by the radius for biconic 1 was toleranced. In fact, the chosen ratio tolerances had the most impact on instrument performance (tolerance sensitivity). They may get adjusted pending discussions with vendors. Once the biconics are fabricated and radii of curvature are measured, the optical prescription, and thus location, of optics will be adjusted to account for the as-built biconic radii. Table 3 gives the tolerances for the biconics. A sensitivity analysis of the design for each tolerance was performed within ZEMAX. The detector position was the sole compensator. Its position was optimized within an allowable ± 1 mm movement range about nominal. Table 4 lists tolerances with the most effect on performance.

Figure 3 is a plot of ZEMAX calculated wavefront error and strehl ratio, on-axis and off-axis (at the middle of the detector edges), sorted in order of performance, for a 100-iteration Monte-Carlo tolerancing run. Since the system at the 90th percentile had performance well within the required 5 % on-axis strehl degradation the optical tolerances should be satisfactory. The optimized detector positions for all 100 iterations, distributed within the allowable tolerance of ± 1 mm, had a 0.60 mm standard deviation around the nominal position.

3. FILTERS

The 5.1 μm-cutoff HgCdTe array establishes the longest practical operating wavelength for LMIRcam. The array has good quantum efficiency to wavelengths as short as 1 μm; however, LMIRcam will operate in a primary

[‖] International Intellectual Group, Inc.

Downloaded from SPIE Digital Library on 13 Jul 2011 to 150.135.115.80. Terms of Use: http://spiedl.org/terms

Table 4. Sensitivity Tolerance Worst Offenders

Tolerance	**Value**	**% Wavefront Error Change**
Ratio of Radii Biconic 2	0.001 (−0.001)	32.5 (32.5)
Ratio of Radii Biconic 1	0.0005 (−0.0005)	28.8 (28.4)
Y-Radius Biconic 1	0.645 mm (−0.645 mm)	16.3 (11.9)
Zernike 8 (Coma) Biconic 1	−50 nm (50 nm)	14.5 (6.2)
Zernike 7 (Coma) Biconic 1	−50 nm	10.2
Y-Conic Constant Biconic 2	−0.05 mm (0.05 mm)	9.1 (8.9)
X-Conic Constant Biconic 2	−0.05 mm (0.05 mm)	8.9 (8.8)
Surface Irregularity Fold 1	29 nm (−29 nm)	7.5 (4.9)
Zernike 10 (Trefoil) Biconic 1	−50 nm (50 nm)	5.9
Zernike 9 (Trefoil) Biconic 1	50 nm	5.7
Zernike 6 (Astigmatism) Biconic 1	50 nm (−50 nm)	3.8 (3.7)
Zernike 5 (Astigmatism) Biconic 1	50 nm	3.8
Surface Figure Fold 1	−0.855 (0.855) fringes at He-Ne	3.4 (2.0)
Zernike 8 (Coma) Biconic 2	50 nm	2.0
Tilt Y Fold 1	−0.0167 deg (0.0167 deg)	1.6 (1.2)
Tilt Y Biconic 1	0.0167 deg	1.3

wavelength range of 2.9 – 5.2 μm due to the declining improvement in Strehl toward shorter wavelengths, the need for diverting K-band light for fringe tracking, and the desire not to duplicate the K-band capabilities of the LBT's near-infrared interferometric imaging instrument, LINC-NIRVANA.[9] The definition of the LMIRcam initial filter set is aimed towards specific scientific goals while also attempting to maximize throughput and minimize the effects of atmospheric absorption. To that end, LMIRcam is primarily an L- and M-band broadband imager/grism spectrograph with specialized filters for PAH, Brackett-α, and water ice band imaging. The choice of bandpass within the traditional broadband windows minimizes contamination from thermal radiation and maximizes atmospheric transmission. Table 5 summarizes the primary filters for initial LMIRcam operation. The table also identifies whether the filter is a stock item available from NDC Infrared (developed as part of a past filter consortium purchased organized by Alan Tokunaga) or a custom filter to be fabricated by Barr Associates. Specifications for the custom filters will closely follow those in Ref. 10.

Table 5. LMIRcam Filter Set. Filters from NDC Infrared are stock items developed as part of a past astronomy filter consortium purchase. Filters from Barr Associates will be custom.

Filter	**Wavelength** (μm)	**Center** (μm)	**Width** (μm)	**Vendor**
L-Band	3.45 – 4.00	3.73	0.55	Barr Associates
M-Band	4.60 – 5.00	4.80	0.40	Barr Associates
H_2O Ice	2.97 – 3.13	3.05	0.16	NDC Infrared
PAH	3.27 – 3.33	3.30	0.06	Barr Associates
L Narrowband cont.	TBD	–	–	Barr Associates
Br-α	4.02 – 4.08	4.05	0.06	NDC Infrared
Br-α cont.	3.95 – 4.01	3.98	0.06	NDC Infrared

Downloaded from SPIE Digital Library on 13 Jul 2011 to 150.135.115.80. Terms of Use: http://spiedl.org/terms

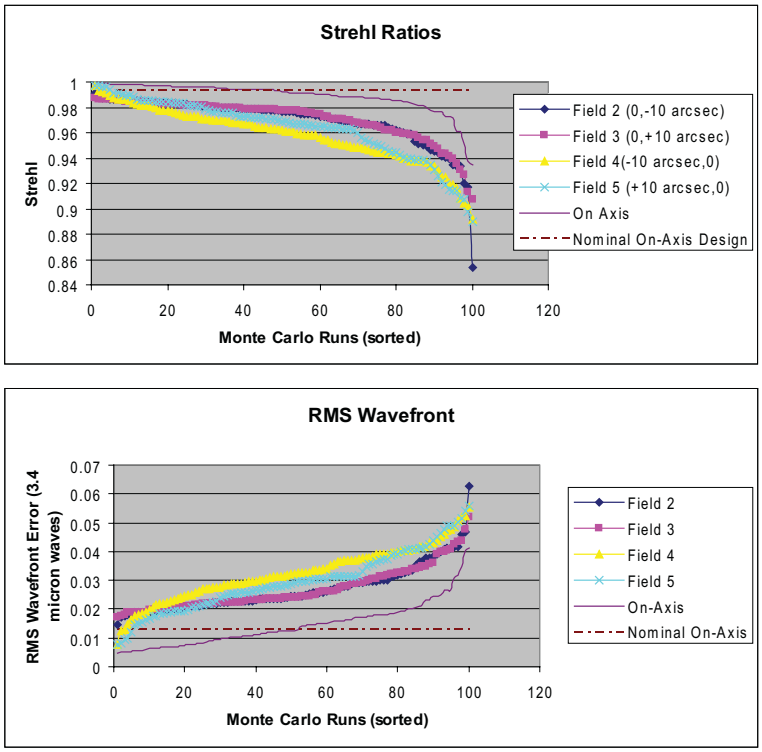

Figure 3. Plots of ZEMAX calculated wavefront error and strehl ratio, on-axis and off-axis (at the middle of the detector edges), sorted in order of performance, for a 100-iteration Monte-Carlo tolerancing run.

3.1 Broadband Filters

3.1.1 L-band

The wavelength region 3.0 – 4.2 μm provides a relatively clean atmospheric window. The LMIRcam L-band filter will be centered on the best atmospheric transmission in this window. It will be similar to the MKO L' filter[10] except for a shorter long-wave cut-off (Figure 4). This choice minimizes atmospheric emissivity and maximizes calibration stability. A forest of narrow, mostly unsaturated, water lines lies at the short end of the window with the worst absorption shortward of 3.4 μm setting the short end. CO_2 dominates the absorption at the long end of the window. Since this species is well-mixed and slowly varying, this absorption primarily influences emissivity rather than calibration. The Brackett-α line at 4.05 μm will be excluded from the LMIRcam L-band filter because the instrument will contain a narrowband filter centered on this emission line. Overall, the LMIRcam L-band will extend from 3.45 – 4.00 μm (all quoted wavelengths are one-half peak transmission).

3.1.2 M-band

The LMIRcam M-band filter will also be a custom design optimized to detect warm exoplanets, a primary science driver for LMIRcam. Ref. 11 presented a bandpass optimization for exoplanet detection for the MMT CLIO 5 μm imager operating at the MMT telescope. They found that the SNR peak lies at a wavelength of 4.75 μm with a bandpass of 0.6 μm, which happens to corresponds closely to the cleanest portion of the 4 – 5 μm atmospheric window. To avoid saturating the array in the minimum correlated double sampling time (0.1 sec) the LMIRcam M-band filter will have a slightly narrower bandpass of 0.4 μm (Figure 5).

3.2 Narrowband Filters

The 3 – 5 μm range also contains three prominent narrow-band emission/absorption features: H_2O Ice around 3 μm, PAH at 3.29 μm, and Brackett-α at 4.05 μm (Figure 6). Our chosen bandpasses are typical for these features. The filter set also includes continuum filters.

Downloaded from SPIE Digital Library on 13 Jul 2011 to 150.135.115.80. Terms of Use: http://spiedl.org/terms

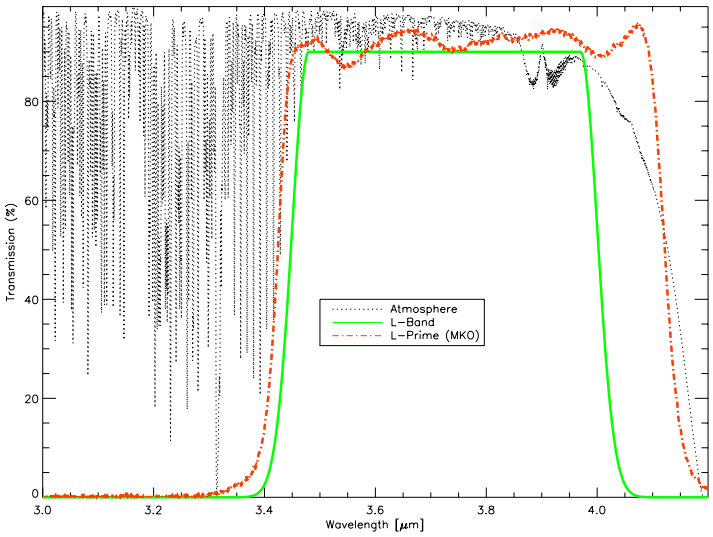

Figure 4. L-band transmission curves. The LMIRcam L-band filter is shown as a solid green curve. The MKO L' filter is plotted for comparison. The black dotted line indicates the atmospheric transmission curve with 1 mm of water column density at 1 airmass.

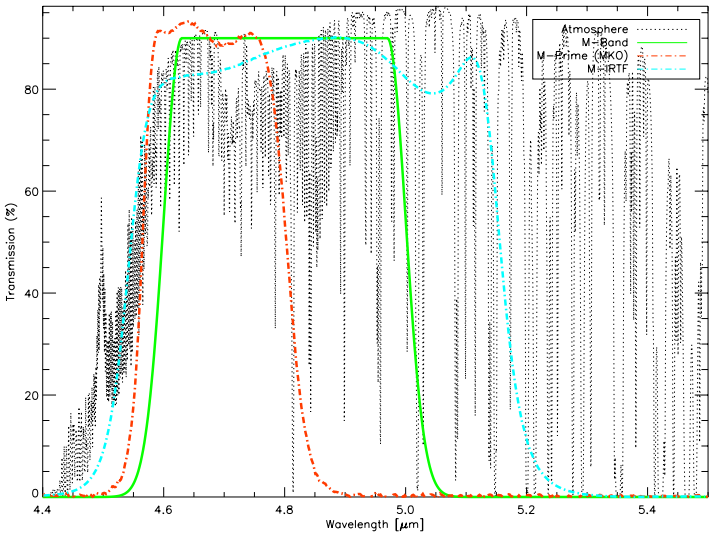

Figure 5. M-band transmission curves showing the proposed LMIRcam M-band filter (solid curve). The M and M' filters from IRTF and the MKO filter set are also shown for comparison.

Downloaded from SPIE Digital Library on 13 Jul 2011 to 150.135.115.80. Terms of Use: http://spiedl.org/terms

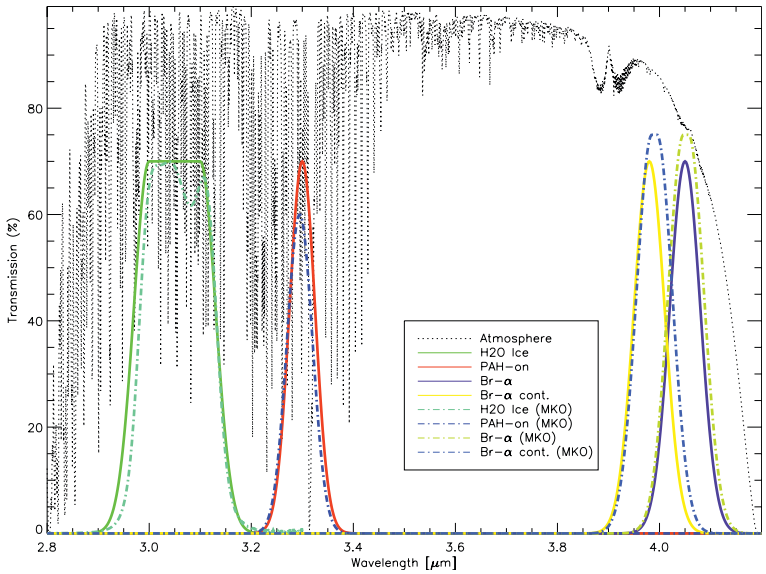

Figure 6. Transmission profiles for the narrow-band filters. As discussed in the text, narrowband continuum filters will also be provided, possibly by providing a CVF.

- **Water Ice** Astronomical water ice absorption is quite wide, with amorphous ice absorption spanning 2.9 – 3.3 μm. The specified LMIRcam filter, available stock from NDC Infrared, is centered on the deepest absorption for typical astronomical ice features (2.97 – 3.13 μm). The breadth of the water ice feature makes continuum comparison difficult, as discussed below.

- **PAH (3.30 μm)** Astronomical PAH emission, typically from UV excitation of small grains in the interstellar medium (ISM), is less than 0.1 μm wide and has a prominent feature centered around 3.29 μm. There is also a narrow PAH feature at 3.30 μm found in regions of altered chemistry such as post-AGB stars. The LMIRcam PAH filter will have a 1.5 % bandwidth (0.05 μm) filter centered at 3.30 μm. This wavelength choice will also allow observations of red-shifted 3.29 μm PAH features in low-z galaxies.

- **L Narrowband Continuum** Both the H_2O and PAH filters require continuum comparison. Attempts to select a wavelength region that could serve as a common continuum for both filters has been difficult. Given the breadth of the H_2O feature, the 3.30 μm filter cannot serve as a valid continuum measurement for a source with H_2O absorption although it may be useful in searches for sources with ice absorption. Wavelengths longward of 3.30 μm, despite good atmospheric transparency, are problematic due to a 3.4 μm PAH feature that often accompanies the one at 3.3 μm, and water ice absorption between 3.2 and 3.6 μm that usually accompanies the 3.1 μm feature. A continuum located at 3.6 μm could be used for both but problems due to unknown continuum slope would be introduced. Locations shortward of 3 μm are problematic because of poor atmospheric transmission and the fact that K-band light is diverted by the dichroic for phase sensing. Either individual H_2O and PAH-continuum filters will be necessary or a circular variable filter (CVF) could be deployed.

- **Brackett-α and Continuum Reference** The narrowband Brackett-α filter is centered on the hydrogen recombination line at 4.05 μm. This emission is intrinsically narrow and the filter, along with the companion continuum filter, have a 1.5 % bandpass, and are available from NDC Infrared.

4. SPECTROSCOPY

LMIRcam will also feature two grisms positioned in the pupil stop wheel just prior to the detector. One grism will deliver R $\sim$ 375 spectra in first order centered at 3.5 μm (L-band) with a groove density of $\sim$ 41.5 lines/mm and a prism/blaze angle of $\sim$ 6 degrees. A second grism will deliver R $\sim$ 385 spectra in first order centered at

Downloaded from SPIE Digital Library on 13 Jul 2011 to 150.135.115.80. Terms of Use: http://spiedl.org/terms

4.85 μm (M-band) with a groove density of $\sim$ 30.7 lines/mm and a prism/blaze angle of 6.2 deg. Appropriate band-pass filters will be used with each grism for order blocking. A filter that passes 2.8 – 4.2 μm light will be used for L-band spectroscopy. The long wavelength cut-off of this filter is necessary to block M-band thermal backgrounds. M-band spectroscopy will use a long-pass filter that cuts-on at 2.8 μm. The slit will be 0.033 arcsec wide on the sky (3 pixel per resolution element sampling) and approx. 8" long, the entire length of the H1RG detector less some pixels at the top and bottom of the array to measure baseline bias.

The grisms will be direct-ruled on either ZnSe or KRS-5 to avoid absorption from resin used in fabrication of replicated grisms.[12] Factors to be considered in making a material choice will include susceptibility to surface degradation during the ruling process which generates scattered light and availability of anti-reflection (AR) coatings for the grism entrance face. The Carl Zeiss company in Jena, Germany, has made multiple KRS-5 direct-ruled grisms recently, including three grisms for 1.5 μm spectroscopy in FLITECAM for SOFIA,[13] and two N-band grisms for the FORCAST instrument on SOFIA.[14] The Bach Research Corp. can direct-rule either ZnSe or KRS-5**.

5. CORONAGRAPHY

Given the anticipated high strehl of the images, coronagraphy will further suppress the Airy fringes of the Fizeau images at image radii greater than the focal plane coronagraphic spot radius of order 2λ/D. Because of significant thermal background at these wavelengths, diffraction suppression will not substantially increase signal-to-noise due to photon noise or atmospheric speckle variations. However, PSF substraction is typically limited to slowly changing optical aberrations. Scattered light from these aberations interfere with the diffracted light to create semi-static speckles in the focal plane. A recent attempt with the MMT demonstrated a 5σ limit delta magnitude limit of 10.5 at M-band[15] for an angular distance of 1 arcsec (5λ/D). In this context, the benefit of coronagraphic suppression at thermal infrared wavelengths is to limit the amount of energy in the diffraction pattern to reduce the brightness of semi-static speckles.

The scattered light in typical M-band adaptive optics (AO) images is 10 % of the light distributed in a halo similar to the Airy pattern. The diffraction "rings" in an image interfere with the scattered light to create a varying background. To eliminate this effect a reduction of the diffraction by roughly a factor of 100 is required, and such performance can be realized by a range of coronagraphic implementations that utilize pupil plane phase manipulations,[16,17] or a combination of focal plane masks and pupil plane stops.[18] The pupil plane phase masks of Ref. 17 can be placed at either pupil but initially they will be placed at the first pupil.

6. MECHANICS

LMIRcam will be integrated into the NIC Dewar which was designed to include extra room for an infrared channel optimized for L- and M-band operation. Figure 7 and Figure 8 show the mechanical design for the NIC/LMIRcam system. The design is modular in the sense that NIC and LMIRcam opto-mechanical assemblies attach to independent structural layers (aluminum plates) within the Dewar. This has the important benefit that the LMIRcam opto-mechanical train can be assembled and aligned independent of the NIC optics. Cryogenic cooling is provided by a two-stage closed cycle system. Cooling of the LMIRcam array and optics derives from the robust first-stage of this system which can deliver 30 W of cooling power at 60 K while still maintaining a second-stage temperature of 6 K needed for the long-wavelength NIC array.

The opto-mechanical design folds around both sides of an "optical bench" (Figure 9). The mechanical implementation benefited substantially from the availability of pre-existing filter/aperture wheel designs (shown in Figure 8) used in other University of Arizona instruments. Sufficient space is available within LMIRcam to accommodate these mechanisms which will be driven by warm motors with vacuum feed-throughs from outside the Dewar.

**B. Bach, private communication

Downloaded from SPIE Digital Library on 13 Jul 2011 to 150.135.115.80. Terms of Use: http://spiedl.org/terms

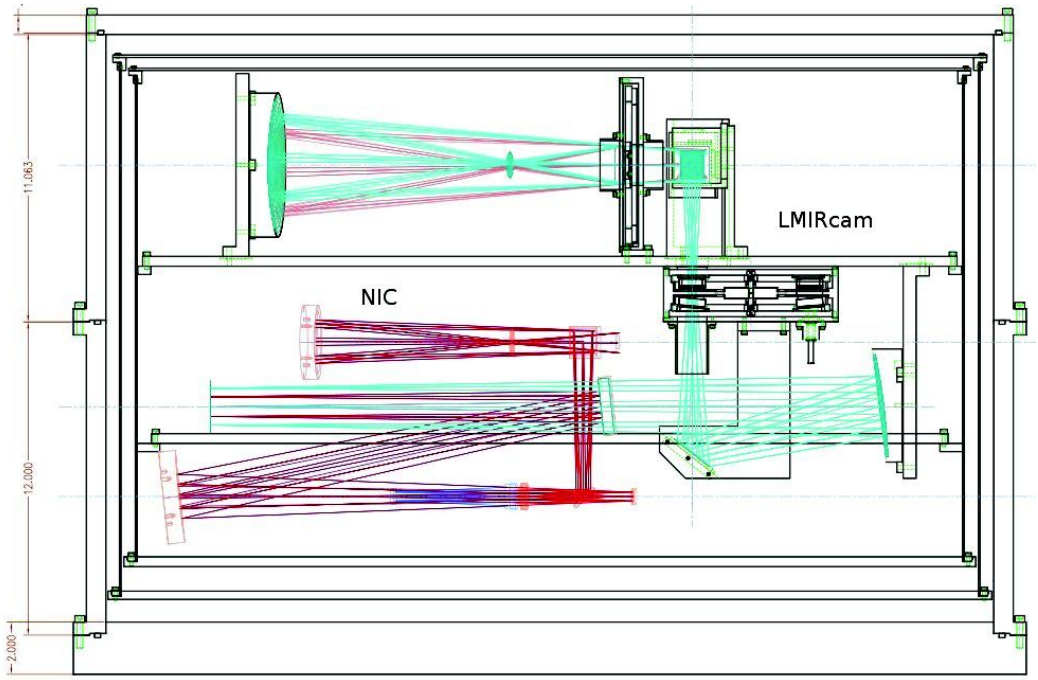

Figure 7. Side view of the LMIRcam (and NIC) mechanical layout. Each imaging system occupies an independent modular layer inside the Dewar.

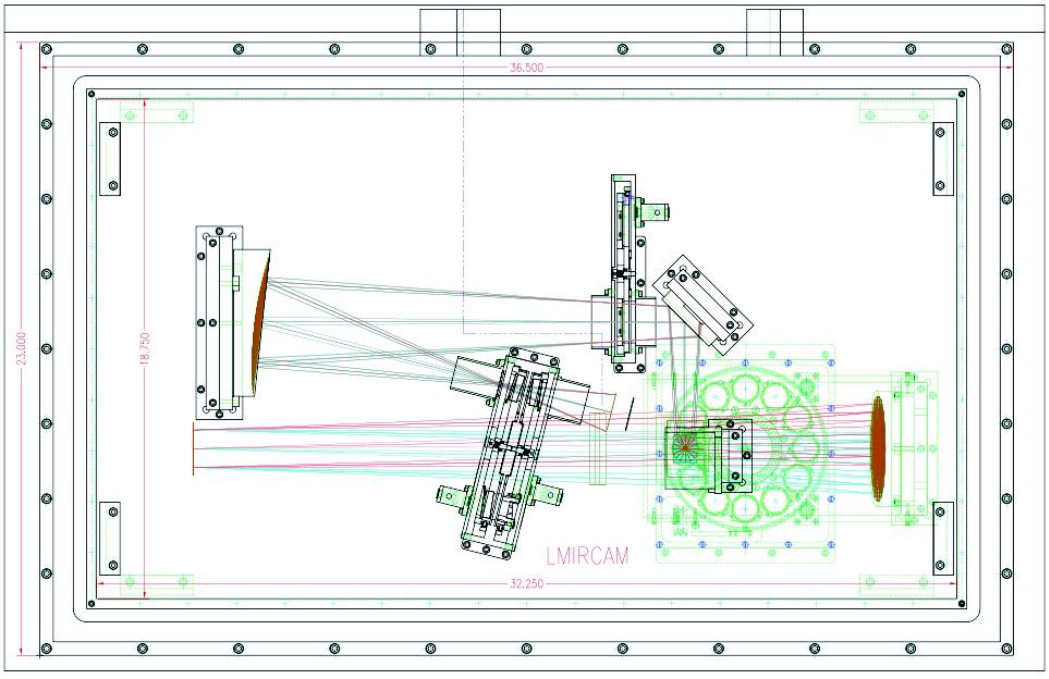

Figure 8. Top view of the mechanical layout (including Dewar wall) with filter and aperture wheels.

Downloaded from SPIE Digital Library on 13 Jul 2011 to 150.135.115.80. Terms of Use: http://spiedl.org/terms

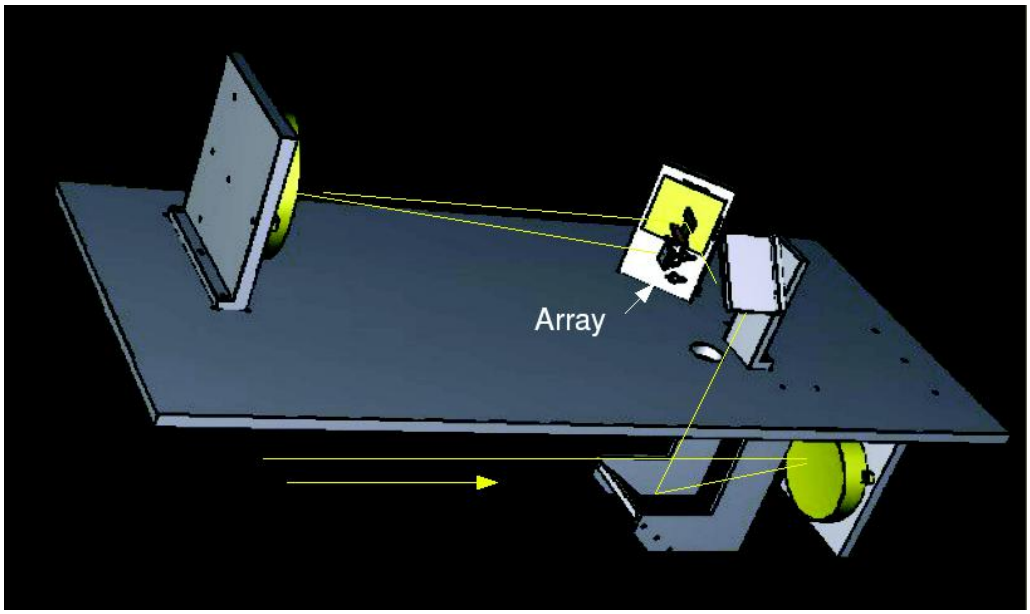

Figure 9. Folded design in perspective relative to the optical bench with filter wheels and focal plane wheel removed.

6.1 Alignment

An all-reflective design with aluminum mirrors fully packaged on the optical bench will allow the system to be assembled and tested warm and cooled to cryogenic temperatures with a high degree of confidence that alignment will be maintained. The mirror substrates and mounting sub-assemblies will be designed to minimize flexure and distortion of the optical surface figure from mechanical stresses. The optics vendor will lap mounting surfaces on both the optics and mounting brackets to reduce tip-tilt errors. Precision dowel pins will also be incorporated in the optics mounting design to aid alignment.

Opto-mechanical testing will be accomplished in stages. Fiducial marks incorporated into the optical bench structure and diamond turned mirrors will be used with lasers to check individual mirror positioning. Resources permitting, alignment techniques and tools such as theodelites for angular measurements and cathetometers for spacing measurements will be used.[8,19]

After integration with NIC at the Univ of Arizona, test facilities for the 10 μm optics will be used for the LMIRcam optics. Instead of a 10 μm CO_2 laser, a 3.39 μm He-Ne laser will provide coherent artificial light to feed each arm of the interferometer to verify overall system alignment. Lastly, on-telescope tests similar to those used for NIC will be performed to integrate LMIRCAM optics with the UBC and LBT.

7. DETECTOR & ELECTRONICS

The Teledyne Imaging Sensors Focal Plane Array will be controlled by high-speed FPGA-based electronics developed by Cornell University[20] for use with the FORCAST first-light SOFIA imager.[21] Our decision to use this controller for LMIRcam's array was driven by an estimated worst-case background rate of 3.4×10^5 e^-/s/pixel (bandpass of 4.5 – 5.1 μm; 15 % surface emissivity at T = 283 K). The mid-wave detector array well-depth of $\sim6\times10^4$ e^- then dictates a minimum frame rate of 10 Hz (FPS) to stay below 1/2 well levels. A HAWAII-1RG array, operating at its fast pixel rate of 5MHz using all 16 available outputs can be read out at 70 frames-per-second (FPS) or 35 FPS in correlated double sampling (CDS) mode. The Cornell/FORCAST 16-channel FPGA based data system can operate at these rates. The array controller will be hosted in a stand alone box co-located with the other NIC array controllers. Data connection to the array will then occur over a dedicated fiber optic link to a hosting computer.

Downloaded from SPIE Digital Library on 13 Jul 2011 to 150.135.115.80. Terms of Use: http://spiedl.org/terms

FORCAST's 14-bit ADCs, one for each of 16 channels, provide adequate dynamic range to sample the array without compromising noise even under low-background conditions. Although the ADC's are capable of running at 5Mhz, it is expected that internal data handling restrictions will lower this rate to around 4MHz allowing a frame rate of about 60 Hz, much faster than our 10 Hz requirement. The 60 Hz frame rate presumes frame co-addition will occur within the instrument electronics.

8. ANTICIPATED PERFORMANCE & SCIENCE APPLICATIONS

At 3.6μm the LBT's first interferometric null lies at a radius of 26 mas from the image centroid. The accompanying small PSF solid angle "footprint" minimizes thermal background radiation and allows LBT to achieve $3 - 5\,\mu$m spatial resolution comparable to the Hubble Space Telescope at visible wavelengths, 100 times better than the Spitzer Space Telescope, and point source sensitivity comparable to space based observatories. Flux limits in one hour of integration (5σ) of 2 μJy at 3.6 μm and 20 μJy at 4.8 μm corresponding to Vega magnitudes of 20.5 and 17.3 are anticipated. Spectroscopic sensitivity is expected to be 2.5 magnitudes brighter. As Table 6 summarizes, the science potential for LMIRcam is rich and varied. LMIRCam will be capable of detecting young warm Jupiters and older "super"-Jupiters around nearby stars. In addition, this wavelength regime provides particular leverage for studying regions of high interstellar extinction, detecting warm dust, 3.3 μm PAH emission, ice feature absorption, and Brackett-α emission.

Table 6. LMIRcam Science Opportunities

Distance	**Scale to first null**	**Science possibility**
2-10AU	40-200 km	Resolved asteroids, Io volcanoes, cometary near-nucleus Jovian H3+ auroral emission
10-500 pc	0.3-15 A.U.	Warm Jupiters around Nearby Stars Circumstellar Disks around Solar Mass stars, Brown Dwarfs
2-10 Kpc	60-300 A.U.	Massive star formation in the MW
1-10 Mpc	0.15-1.5 pc	Star Formation in the Local Universe
z=0.1-0.5+	50-250 pc	Local Starburst Galaxies, AGN, ULIRGs

LMIRcam capability will provide significant support and follow-up for the Atacama Large Millimeter Array (ALMA) which will begin operating in 2010 and the Wide Field Infrared Survey Explorer (WISE), scheduled for launch in late 2009. LMIRcam complements ALMA with similar spatial resolution while being able to detect and potentially resolve the sources cataloged by the all-sky WISE mid-infrared survey mission.

9. ACKNOWLEDGEMENTS

We thank Ray Ohl for numerous discussions regarding the procurement and use of biconic mirrors in astronomical instruments. We thank James Sutter for advice on Zemax and Alex Sohn and Thomas Dow for information about manufacturing biconic mirrors and a tour of the NC State Precision Engineering Center. We thank Gary Peterson for helpful discussions about scattered light. We also thank members of the LBT community, especially Kris Sellgren and Mike Meyer, for helpful comments regarding filter selection. The University of Virginia provided funds to purchase the infrared array. This material is based upon work supported by the National Science Foundation under Grant No. 0705296.

REFERENCES

[1] Hinz, P.M. et al., "Status of the LBT interferometer," in [*Optical and Infrared Interferometry*], Schöler, M., Danchi, W. C., and Delplancke, F., eds., *Proc. SPIE* **7013**, 79 (2008).

Downloaded from SPIE Digital Library on 13 Jul 2011 to 150.135.115.80. Terms of Use: http://spiedl.org/terms

[2] Hinz, P. M., Durney, O. F., Solheid, E., and Hoffmann, W. F., "NIC: LBTI's nulling and imaging camera," in [*Optical and Infrared Interferometry*], Schöler, M., Danchi, W. C., and Delplancke, eds., *Proc. SPIE* **7013**, 119 (2008).

[3] Ohl, R. G., Dow, T. A., Sohn, A., and Garrard, K., "Highlights of the ASPE 2004 Winter Topical Meeting on Free-Form Optics: Design, Fabrication, Metrology, Assembly," in [*Optical Fabrication, Metrology, and Material Advancements for Telescopes*], Atad-Ettedgui, E. and Dierickx, P., eds., *Proc. SPIE* **5494**, 49 (2004).

[4] Ohl, R. G., Preuss, W., Sohn, A., Conkey, S., Garrard, K. P., Hagopian, J. G., Howard, J. M., Hylan, J. E., Irish, S. M., Mentzell, J. E., Schroeder, M., Sparr, L. M., Winsor, R. S., Zewari, S. W., Greenhouse, M., and MacKenty, J. W., "Design and fabrication of diamond machined, aspheric mirrors for ground-based, near-IR astronomy," in [*Instrument Design and Performance for Optical/Infrared Ground-based Telescopes*], Iye, M. and Moorwood, A. F. M., eds., *Proc. SPIE* **4841**, 677 (2003).

[5] Bennett, J. M. and Mattsson, L., [*Introduction to Surface Roughness and Scattering, 2nd Edition*], Optical Society of America, Washington, D.C. (1999).

[6] Noll, R. J., "Zernike polynomials and atmospheric turbulence," *J. Opt. Soc. Am.* **66**, 207 (1976).

[7] Ohl, R. G., Barthelmy, M. P., Zewari, S. W., Toland, R. W., McMann, J. C., Puckett, D. F., Hagopian, J. G., Hylan, J. E., Mentzell, J. E., Mink, R. G., Sparr, L. M., Greenhouse, M. A., and MacKenty, J. W., "Comparison of stress relief procedures for cryogenic aluminum mirrors," in [*Cryogenic Optical Systems and Instruments IX*], Heaney, J. B. and Burriesci, L. G., eds., *Proc. SPIE* **4822**, 51–71 (2002).

[8] Connelly, J. A., Ohl, R. G., Saha, T. T., Hadjimichael, T., Mentzell, J. E., Mink, R. G., , Hylan, J. E., Sparr, L. M., Chambers, V. J., Hagopian, J. G., Greenhouse, M. A., Winsor, R. S., and MacKenty, J. W., "Imaging performance and modeling of the Infrared Multi-Object Spectrometer focal reducer," in [*Instrument Design and Performance for Optical/Infrared Ground-based Telescopes*], Iye, M. and Moorwood, A. F. M., eds., *Proc. SPIE* **4841**, 702 (2003).

[9] Herbst, T. M., Ragazzoni, R., Eckart, A., and Weigelt, G., "The linc-nirvana interferometric imager for the large binocular telescope," in [*Ground-based Instrumentation for Astronomy*], Moorwood, A. F. M. and Iye, M., eds., **5492**, 1045 (2004).

[10] Tokunaga, A. T., Simons, D. A., and Vacca, W. D., "The Mauna Kea Observatories Near-Infrared Filter Set. II. Specifications for a New $JHKL'M'$ Filter Set for Infrared Astronomy," *PASP* **114**, 180 (2002).

[11] Freed, M., Hinz, P. M., Meyer, M. R., Milton, N. M., and Lloyd-Hart, M., "Clio: A 5 micron camera for the detection of giant exoplanets," in [*Ground-based Instrumentation for Astronomy*], Moorwood, A. F. M. and Iye, M., eds., **5492**, 1561 (2004).

[12] Rayner, J. T., "Evaluation of a solid KRS-5 grism for infrared astronomy," in [*Infrared Astronomical Instrumentation*], Fowler, A. M., ed., *Proc. SPIE* **3354**, 289–294 (1998).

[13] Smith, E. C. and McLean, I. S., "Grism spectroscopy with FLITECAM," in [*Ground-based and Airborne Instrumentation for Astronomy*], McLean, I. S. and Iye, M., eds., *Proc. SPIE* **6269**, 62691I (2006).

[14] Ennico, K. A., Keller, L. D., Mar, D. J., Herter, T. L., Jaffe, D. T., Adams, J. D., and Greene, T. P., "Grism performance for mid-IR (5-40 micron) spectroscopy," in [*Ground-based and Airborne Instrumentation for Astronomy*], McLean, I. S. and Iye, M., eds., *Proc. SPIE* **6269**, 62691Q (2006).

[15] Hinz, P. M., Heinze, A. N., Sivanandam, S., Miller, D. L., Kenworthy, M. A., Brusa, G., Freed, M., and Angel, J. R. P., "Thermal infrared constraint to a planetary companion of vega with the mmt adaptive optics system," *ApJ* **653**, 1486–1492 (2006).

[16] Codona, J. L., "Exoplanet imaging with the Giant Magellan Telescope," in [*Advancements in Adaptive Optics*], Calia, D. B., Ellerbroek, B. L., and Ragazzoni, R., eds., *Proc. SPIE* **5490**, 379–388 (2004).

[17] Kenworthy, M. A., Codona, J. L., Hinz, P. M., Angel, J. R. P., Heinze, A., and Sivanandam, S., "First on-sky high-contrast imaging with an apodizing phase plate," *ApJ* **660**, 762–769 (2007).

[18] Grover A. Swartzlander, J., "Achromatic optical vortex lens," *Optics Letters* **31**, 2042 (2006).

[19] Hagopian, J. G., Hayes, P., Crooke, J., and Lyons, J., "Optomechanical alignment of the composite infrared spectrometer (cirs) for the cassini mission to saturn," in [*Cryogenic Optical Systems and Instruments VII*], Burriesci, L. G. and Heaney, J. B., eds., **2814**, 46 (1996).

Downloaded from SPIE Digital Library on 13 Jul 2011 to 150.135.115.80. Terms of Use: http://spiedl.org/terms

[20] Pirger, B. E., Schoenwald, J., Herter, T. L., Gull, G. E., Adams, J. D., Keller, L. D., Berthoud, M., Henderson, C., Stacy, G. J., and Nikola, T., "High-speed highly-flexible reconfigurable data acquisition system for astronomy," in [*High Energy, Optical, and Infrared Detectors for Astronomy II*], Dorn, D. A. and Holland, A. D., eds., *Proc. SPIE* **6276**, 62760X (2006).

[21] Keller, L. D., Herter, T., Stacey, G., Gull, G., Schoenwald, J., Pirger, B., Adams, J., Berthoud, M., and Nikola, T., "First test results from forcast: the facility mid-ir camera for sofia," in [*Ground-based Instrumentation for Astronomy*], Moorwood, A. F. M. and Iye, M., eds., **5492**, 1086–1093 (2004).

Downloaded from SPIE Digital Library on 13 Jul 2011 to 150.135.115.80. Terms of Use: http://spiedl.org/terms